

Double magnetic transitions, complex field induce phases, and large magnetocaloric effect in the frustrated garnet compound $\text{Mn}_3\text{Cr}_2\text{Ge}_3\text{O}_{12}$

S. Mohanty,^{1,*} A. Magar,^{1,*} Vikram Singh,¹ S. S. Islam,¹ S. Guchhait,¹ A. Jain,² S. M. Yusuf,² and R. Nath^{1,†}

¹*School of Physics, Indian Institute of Science Education and Research Thiruvananthapuram-695551, India*

²*Solid State Physics Division, Bhabha Atomic Research Centre, Mumbai 400 085, India*

(Dated: March 5, 2024)

A detailed study of the structural and magnetic properties of a garnet compound $\text{Mn}_3\text{Cr}_2\text{Ge}_3\text{O}_{12}$ is carried out using x-ray diffraction, magnetization, heat capacity, and neutron diffraction measurements. This compound manifests two successive magnetic transitions at $T_{N1} \simeq 4.5$ K and $T_{N2} \simeq 2.7$ K. Neutron powder diffraction experiments reveal that these two transitions correspond to the orderings of Cr^{3+} and Mn^{2+} sub-lattices, respectively. The ordering at T_{N1} is found to be collinear antiferromagnetic type while the one at T_{N2} is of non-collinear antiferromagnetic type. There appears to be several interactions, both ferromagnetic and antiferromagnetic, between two sub-lattices yielding a three-dimensional frustrated pyrochlore geometry. The $H - T$ phase diagram is quite complex and displays multiple phases under magnetic field which can be attributed to the frustrated nature of the spin-lattice. Moreover, it shows a large magnetocaloric effect at low temperatures with a maximum value of isothermal entropy change $\Delta S_m \simeq -23$ J/kg-K and adiabatic temperature change $\Delta T_{ad} \simeq 9$ K for a field change of 7 T. Further, a large value of relative cooling power ($RCP \simeq 360$ J/kg) reflects the usefulness of the compound in magnetic refrigeration purpose.

I. INTRODUCTION

Frustrated magnets are widely studied because of their potential to host a variety of exotic ground states [1, 2]. In particular, the geometrically frustrated magnets in three-dimension (3D) that include pyrochlore and hyperkagome lattices made up of corner-sharing tetrahedra and corner-sharing triangles, respectively have the most intricate ground states [3, 4]. Garnet is a family of compounds with general formula $A_3B_2C_3O_{12}$ which can accommodate a large variety of chemical constituents. Here, A , B , and C occupy the dodecahedral, octahedral, and tetrahedral crystallographic sites, respectively [5]. This family of garnets provides a convenient platform to observe wide variety of non-trivial properties by introducing different ($3d$ and $4f$) magnetic ions at different crystallographic sites. For instance, the magnetic ion only at the A -site forms a geometrically frustrated hyperkagome lattice. Thus, with a $3d$ magnetic ion at the A -site, the hyperkagome lattice may feature complex magnetic structures as in $\text{Co}_3\text{Al}_2\text{Si}_3\text{O}_{12}$ [6] and also fascinating phenomenon like magnetoelectric effect as in $\text{Mn}_3\text{Al}_2\text{Ge}_3\text{O}_{12}$ [7]. Similarly, $4f$ ions occupying the A -site shows very peculiar low temperature features. For example, the celebrated garnet compound $\text{Gd}_3\text{Ga}_5\text{O}_{12}$ manifests quantum-spin-liquid with a hidden long-range-order (LRO) [8], $\text{Tb}_3\text{Ga}_5\text{O}_{12}$ exhibits a field induced LRO [9], $\text{Ho}_3\text{Ga}_5\text{O}_{12}$ shows a disordered ground state etc [10].

Another class of garnets can be obtained by introducing either same or different magnetic ions at both B and C sites. One such family is $R_3\text{Fe}_5\text{O}_{12}$ (where

R is a rare-earth ion) which has received wide attention because of the ferrimagnetic ground state. In these compounds, Fe substitution at two crystallographic sites introduces strong inter-sublattice interaction, resulting in many interesting properties [11]. Among them, $\text{Y}_3\text{Fe}_5\text{O}_{12}$ is a well-studied compound that displays ferrimagnetism, magnetoelectric effect, and thermal spin dynamics [12, 13]. One can also unfold further excitations in the magnetic properties of the garnets by substituting two different magnetic ions at the A and B sites. It would be engrossing to study how the intra- and inter-sublattice interactions shape the magnetic ground state of these systems. This may also introduce strong frustration either due to frustrated geometry or competing antiferromagnetic (AFM) and ferromagnetic (FM) interactions. In this category, only a few compounds are reported with very preliminary magnetic measurements. For instance, $\text{Mn}_3\text{Fe}_2\text{Ge}_3\text{O}_{12}$ undergoes an AFM ordering at around 6 K [14] while $\text{Mn}_3\text{Cr}_2\text{Ge}_3\text{O}_{12}$ shows the onset of two AFM orderings at low temperatures [15, 16].

Moreover, frustrated magnets owing to their large magnetocaloric effect (MCE) are considered as model systems for magnetic refrigeration [17]. Magnetic refrigeration uses adiabatic demagnetization technique to achieve low temperatures which is an environment-friendly replacement for gas compression technique used in standard refrigerators for room temperature applications and a cost-effective replacement to achieve sub-Kelvin temperatures over expensive ^3He and ^4He . To attain low temperatures using MCE, magnets with low transition temperatures and large entropy change are desirable. Magnetic frustration can suppress the magnetic ordering and induce large entropy change [18]. Theoretically, garnets are predicted to have the potential to cool down to lower temperatures than the paramagnets because of the frustration introduced by the unique structure of this family [18]. Indeed, $\text{Gd}_3\text{Ga}_5\text{O}_{12}$ gadolinium gallium garnet (GGG)

* These authors have equal contribution

† nath@iisertvm.ac.in

exhibits a giant MCE with isothermal entropy change of ~ 450 J/kg K and one can achieve temperatures as low as 800 mK [19]. Therefore, GGG is commercially used in majority of the magnetic refrigerators. Similarly, few other compounds from the garnet family are reported to show large cooling power and one can achieve temperatures in the milli-Kelvin range [19]. Further, garnets are also proved to be very useful in technological applications. For instance, neodymium-doped garnets are good laser materials, ferrimagnetic garnets have applications in electronic devices etc [20].

In the present work, we re-visited and probed the magnetic properties of the garnet compound $\text{Mn}_3\text{Cr}_2\text{Ge}_3\text{O}_{12}$ (MCGO) in detail by means of magnetic, thermodynamic, neutron diffraction, and magnetocaloric measurements. MCGO is reported to crystallize in a cubic structure with space group $Ia\bar{3}d$ (No. 230) at room temperature [21]. Here, Mn^{2+} ion is situated in a dodecahedral site coordinated with eight oxygen atoms, Cr^{3+} is forming octahedra with six oxygen atoms, and Ge^{4+} is forming slightly distorted tetrahedra with four oxygen atoms as shown in Fig. 1(a). CrO_6 octahedron are corner shared with GeO_4 tetrahedra making a 3D structure with a shortest Cr-Cr distance ~ 5.1962 Å. Similarly, MnO_8 units are directly edge shared to make a frustrated hyper-kagome lattice with a shortest Mn-Mn distance of ~ 3.6742 Å, though additional interactions via GeO_4 are also possible. The Mn^{2+} and Cr^{3+} sub-lattices are further coupled with each other as shown in Fig. 1(d), resulting in a pyrochlore-like structure with a shortest Mn^{2+} - Cr^{3+} bond length ~ 3.3541 Å. Our measurements divulge double magnetic transitions in zero-field and a complex low temperature phase diagram in magnetic fields. The nature of the ground states in zero-field is determined via powder neutron diffraction experiments. Moreover, a large MCE is obtained across the transitions.

II. EXPERIMENTAL DETAILS

A polycrystalline sample of MCGO is prepared by conventional solid-state reaction technique by heating stoichiometric mixtures of Mn_3O_4 (Aldrich, 99.99%), Cr_2O_3 (Aldrich, 99.99%), and GeO_2 (Aldrich, 99.99%). These reagents were finely ground, pressed into pellets, and fired at 800 – 1200°C with multiple intermediate regrindings. Finally, green-colored polycrystalline sample of MCGO was obtained. The phase purity of the product was confirmed by powder x-ray diffraction (XRD) recorded at room temperature using a PANalytical x-ray diffractometer ($\text{CuK}\alpha$ radiation, $\lambda_{\text{avg}} \simeq 1.5418$ Å). Figure 2 presents the powder XRD pattern of MCGO along with the Rietveld fit. With the help of Rietveld refinement, all the diffraction peaks of MCGO could be indexed with the cubic unit cell [$Ia\bar{3}d$ (No. 230)], taking the initial structural parameters from Ref. [21]. The absence of any unidentified peak suggests the phase purity of the polycrystalline sample. The obtained lattice parameters

at room temperature are $a = b = c \simeq 12.029(5)$ Å and unit-cell volume $V_{\text{cell}} \simeq 1740.60(1)$ Å³, which are in close agreement with the previous report [21].

Magnetization (M) measurements were performed as a function of temperature ($0.4 \text{ K} \leq T \leq 380 \text{ K}$) and magnetic field ($0 \leq H \leq 7 \text{ T}$) using a superconducting quantum interference device (SQUID) (MPMS-3, Quantum Design) magnetometer. Measurements below 1.8 K and down to 0.4 K were carried out using a ^3He attachment to the MPMS. Heat capacity (C_p) as a function of T ($0.4 \text{ K} \leq T \leq 250 \text{ K}$) and H ($0 \leq H \leq 9 \text{ T}$) was measured on a small piece of sintered pellet using the relaxation technique in the physical property measurement system (PPMS, Quantum Design). Measurements below 1.8 K were carried out using an additional ^3He insert in the PPMS.

To solve the magnetic structure, temperature-dependent ($2.5 \text{ K} \leq T \leq 300 \text{ K}$) neutron powder diffraction (NPD) experiments were carried out using the powder diffractometer at the Dhruva reactor, Bhaba Atomic Research Center (BARC), Mumbai, India. Measurements were carried out using powder-diffractometer PD-I ($\lambda \simeq 1.094$ Å) with three linear position-sensitive detectors. The one-dimensional neutron-depolarization measurements were performed using the polarized neutron spectrometer (PNS) at the Dhruva reactor with a constant wavelength of $\lambda \simeq 1.205$ Å. For these measurements, a Cu_2MnAl Heusler single crystal [(111) reflection] was used to produce the incident polarized neutron beams (along z -direction) and a $\text{Co}_{0.92}\text{Fe}_{0.8}$ [(200) reflection] single crystal was used to analyze the polarization of the transmitted (scattered) beam. A π -flipper placed just before the sample allowed the polarization state of the neutron beam on the powder sample to be controlled between spin-up and spin-down states. The sample was placed in an Al sample holder. The flipping ratio of the beam was determined by measuring the intensities of neutrons in non-spin flip and spin flip channels with the π -flipper on and off, respectively. Rietveld refinement of the powder XRD and NPD data was performed using the FullProf software package [22].

III. RESULTS AND DISCUSSION

A. Magnetization

The measured magnetization data are presented in Fig. 3. Temperature-dependent magnetic susceptibility χ [$\equiv M/H$] measured in different applied fields is shown in Fig. 3(a). It displays two clear anomalies at $T_{N1} \simeq 4.7$ K and $T_{N2} \simeq 2.8$ K in $\mu_0 H = 0.01$ T, reflecting two successive magnetic transitions. With increasing field, both the anomalies are suppressed towards low temperatures, typically expected for an AFM ordering. The inverse susceptibility ($1/\chi$) as a function of temperature [inset of Fig. 3(a)] exhibits a completely linear behavior in the high temperature paramagnetic (PM) regime. For

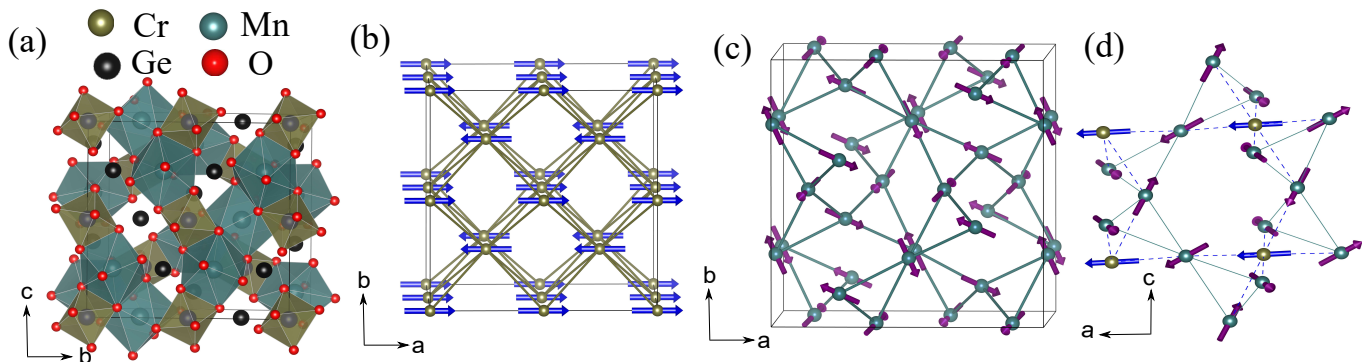


FIG. 1. (a) Three-dimensional view of the crystal structure of MCGO. (b) Arrangement of spins in the Cr^{3+} sub-lattice. (c) Hyperkagome structure formed by the Mn^{2+} ions. (d) Coupling between Mn^{2+} and Cr^{3+} ions that yields pyrochlore-like structure.

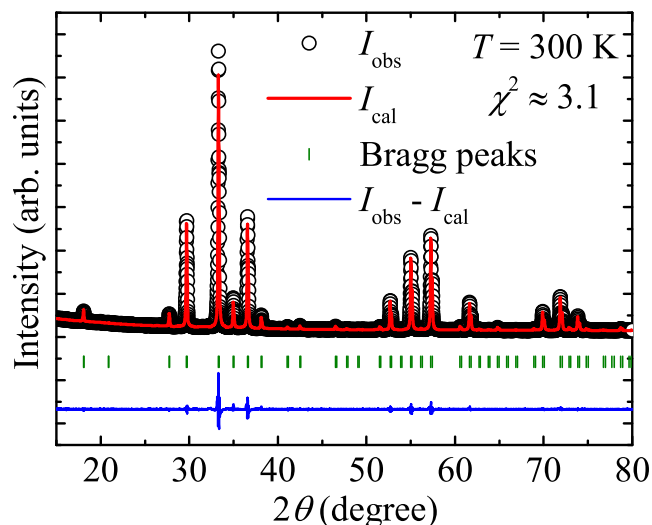


FIG. 2. Powder XRD data collected at room temperature. The red solid line is the Rietveld fit to the data, the vertical bars are the Bragg positions, and the blue line at the bottom is the difference between experimentally observed and calculated intensities.

a tentative estimation of magnetic parameters, we fitted the data above 80 K by the modified Curie-Weiss (CW) law

$$\chi(T) = \chi_0 + \frac{C}{(T - \theta_{\text{CW}})}. \quad (1)$$

Here, χ_0 is the temperature-independent susceptibility, C is the CW constant, and θ_{CW} is the characteristic CW temperature. The fit yields $\chi_0 \simeq -1.79 \times 10^{-5} \text{ cm}^3/\text{mol}$, $C \simeq 16.31 \text{ cm}^3\text{K}/\text{mol}$, and $\theta_{\text{CW}} \simeq -1 \text{ K}$. From the value of C the effective moment is calculated to be $\mu_{\text{eff}} \simeq 11.42 \mu_{\text{B}}$. Theoretically, μ_{eff} for a compound containing two magnetic ions can be calculated as $\mu_{\text{eff}}^2 = n_1\mu_1^2 + n_2\mu_2^2$ where, n_1 and n_2 are the number of magnetic ions present in the compound and μ_1 and μ_2 are their respective spin only magnetic moments [23, 24]. In the formula unit,

MCGO contains $n_1 = 3$ magnetic Mn^{2+} ions with spin $S_1 = 5/2$ and $n_2 = 2$ magnetic Cr^{3+} ions with spin $S_2 = 3/2$. The obtained $\mu_{\text{eff}} \simeq 11.42 \mu_{\text{B}}$ from the CW fit is found to be close to the calculated value of $\mu_{\text{eff}} = 11.61 \mu_{\text{B}}$, considering all these magnetic ions. The small and negative value of θ_{CW} reflects co-existence of FM and AFM interactions with the dominant one being AFM.

Note that the simple CW description is applicable for a system with a well defined single angular momentum ground state and isotropic exchange coupling [25, 26]. In MCGO, we have two sub-lattices made up of Mn^{2+} ($S_1 = 5/2$) and Cr^{3+} ($S_2 = 3/2$) ions, respectively with different exchange couplings and also there exists inter-sublattice interactions. Hence, Eq. (1) is not adequate to give a quantitative description to such a mixed-spin system. Further, double transitions are typically observed in triangular and kagome lattice antiferromagnets having single magnetic ion and with easy-axis anisotropy [27–29]. However, MCGO features a pyrochlore lattice of corner-shared tetrahedra and has two different magnetic ions forming two separate sub-lattices. Hence, the observed double transitions may have different origins. Therefore, we have adopted powder neutron diffraction experiment (discussed later) to pinpoint the actual nature of the spin-spin correlations.

Figure 3(b) presents the χT vs T plot for different applied fields. As one goes down in temperature, χT increases continuously, passes through a maximum around 10 K, and then falls rapidly towards zero. The initial rise and gradual fall are clear signatures of FM and AFM correlations at high and low- T s, respectively [30]. Thus, the coexistence of FM and AFM interactions is inferred from the small negative value of θ_{CW} as well as from the χT behavior.

A magnetic isotherm (M vs H) measured at $T = 0.4 \text{ K}$ is shown in Fig. 3(c). M increases with H , shows slope changes at several intermediate fields, and then a broad plateau or tendency of saturation above $\sim 2.5 \text{ T}$. Even above 2.5 T, M does not saturate completely but exhibits a slow linear increase upto the measured field of 7 T. At

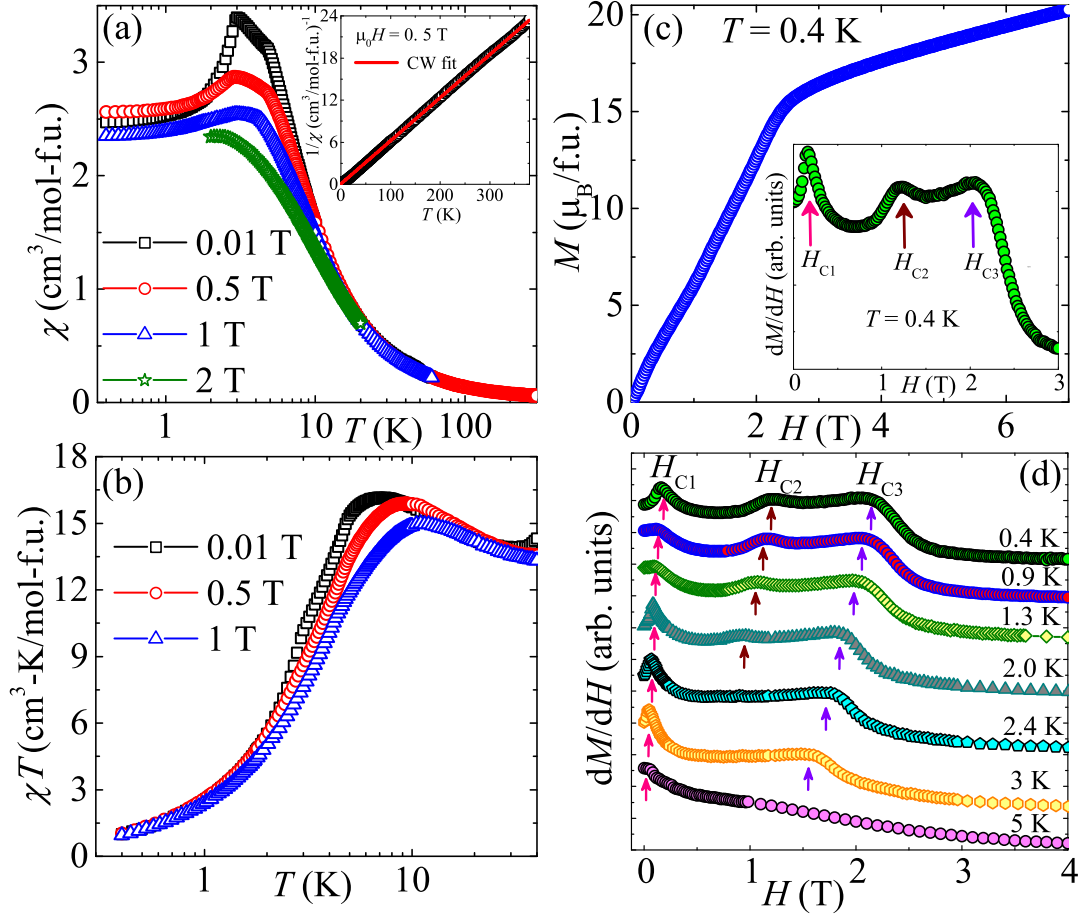


FIG. 3. (a) χ vs T in different fields. Inset: $1/\chi$ vs T for $\mu_0 H = 0.5$ T with the Curie-Weiss fit. (b) χT vs T in different fields. (c) Magnetic isotherm (M vs H) and its derivative in the inset at $T = 0.4$ K. (d) Derivative of isothermal magnetization vs H in different temperatures showing the field induced transitions marked by H_{C1} , H_{C2} , and H_{C3} .

$\mu_0 H = 7$ T, M reaches a value $\sim 20.2 \mu_B/f.u.$ which is still less than the expected saturation magnetization for the entire spin system $M_S = g(n_1 S_1 + n_2 S_2)\mu_B = 21 \mu_B$, taking $g = 2$, $n_1 = 3$, $S_1 = 5/2$, $n_2 = 2$, and $S_2 = 3/2$.

The derivative of magnetization with respect to field (dM/dH) vs H presented in Fig. 3(d) for different temperatures clearly visualize the slope changes at the critical fields H_{C1} , H_{C2} , and H_{C3} . dM/dH at $T = 0.4$ K is shown separately in the inset of Fig. 3(c) for better visualization of these three critical fields. These field-induced features are more pronounced at low temperatures, shift with temperature, and then disappear at high temperatures. Unfortunately, none of these critical fields can be assigned to the saturation field of individual sub-lattices, due to complex network of intra- and inter-sublattice exchange couplings. Thus, the appearance of multiple field-induced transitions indicates strong magnetic frustration in the compound [31].

B. Heat Capacity

Temperature-dependent heat capacity (C_p) measured in zero-field is shown in Fig. 4(a). In a magnetic insulator, the total heat capacity $C_p(T)$ is the sum of two major contributions: phonon contribution $C_{ph}(T)$ which dominates in the high-temperature region and magnetic contribution $C_{mag}(T)$ that dominates in the low-temperature region depending upon the strength of the exchange interactions. In order to extract $C_{mag}(T)$ from $C_p(T)$, first $C_{ph}(T)$ was estimated fitting the high- T C_p data by a linear combination of one Debye [$C_D(T)$] and three Einstein [$C_E(T)$] terms (Debye-Einstein model) as [32–34]

$$C_{ph}(T) = f_D C_D(\theta_D, T) + \sum_{i=1}^3 g_i C_{E_i}(\theta_{E_i}, T). \quad (2)$$

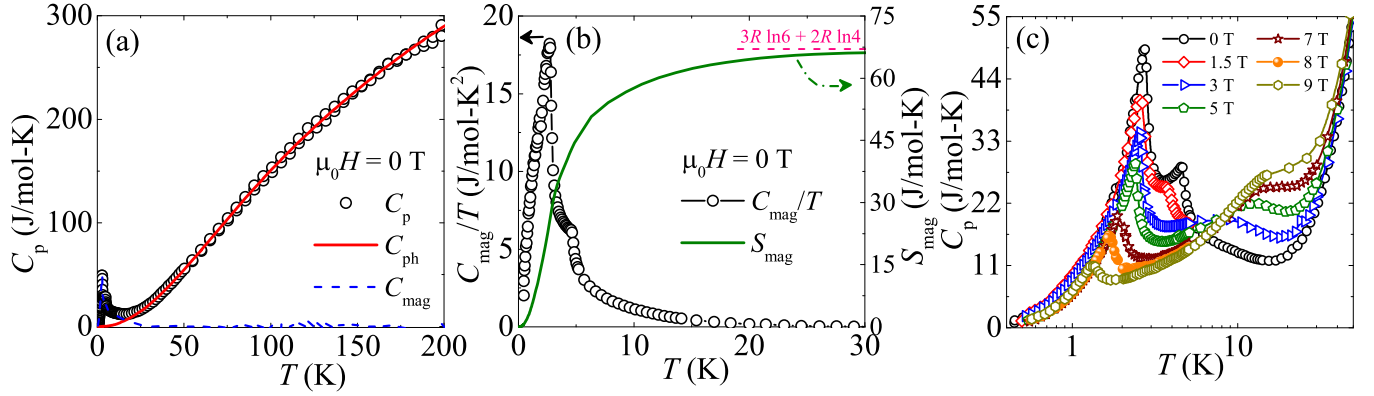


FIG. 4. (a) C_p vs T in zero-field. The red solid line represents the phonon contribution (C_{ph}), while the blue dashed line indicates the magnetic contribution (C_{mag}). (b) C_{mag}/T and S_{mag} vs T in the left and right y-axes, respectively. (c) C_p vs T in the low- T regime measured in different fields.

The first term in Eq. (2) takes into account the acoustic modes, called the Debye term with the coefficient f_D and

$$C_D(\theta_D, T) = 9nR \left(\frac{T}{\theta_D} \right)^3 \int_0^{\frac{\theta_D}{T}} \frac{x^4 e^x}{(e^x - 1)^2} dx. \quad (3)$$

Here, $x = \frac{\hbar\omega}{k_B T}$, ω is the frequency of oscillation, R is the universal gas constant, and θ_D is the characteristic Debye temperature. The second term in Eq. (2) accounts for the optical modes of the phonon vibration, known as the Einstein term with the coefficient g_i and

$$C_E(\theta_E, T) = 3nR \left(\frac{\theta_E}{T} \right)^2 \frac{e^{\frac{\theta_E}{T}}}{[e^{\frac{\theta_E}{T}} - 1]^2}. \quad (4)$$

Here, θ_E is the characteristic Einstein temperature. The coefficients f_D , g_1 , g_2 , and g_3 represent the fraction of atoms that contribute to their respective parts. These values are taken in such a way that their sum should be equal to one. The zero-field $C_p(T)$ data above ~ 20 K are fitted by Eq. (2) [red solid line in Fig. 4(a)] and the obtained parameters are $f_D \simeq 0.06$, $g_1 \simeq 0.18$, $g_2 \simeq 0.37$, $g_3 \simeq 0.39$, $\theta_D \simeq 115$ K, $\theta_{E1} \simeq 170$ K, $\theta_{E2} \simeq 360$ K, and $\theta_{E3} \simeq 700$ K. Finally, the high- T fit was extrapolated down to low temperatures and $C_{mag}(T)$ [blue dashed line in Fig. 4(a)] was estimated by subtracting $C_{ph}(T)$ from $C_p(T)$. Figure 4(b) presents $C_{mag}(T)/T$ and the corresponding magnetic entropy [$S_{mag}(T) = \int_{0.4K}^T \frac{C_{mag}(T')}{T'} dT'$]. The obtained magnetic entropy, which saturates above 20 K, approaches a value $S_{mag} \simeq 67.15$ J/mol-K. This value is close to the expected theoretical values of $S_{mag} = n_1 \times R \ln(2S_1 + 1) + n_2 \times R \ln(2S_2 + 1) = 67.74$ J/mol-K.

At low temperatures, zero-field $C_p(T)$ shows two well-defined anomalies at $T_{N1} \simeq 4.5$ K and $T_{N2} \simeq 2.7$ K, confirming two successive magnetic transitions. To gain more information about the magnetic transitions, we measured $C_p(T)$ in different applied fields [see Fig. 4(c)]. With increasing field, the height of the peaks is reduced

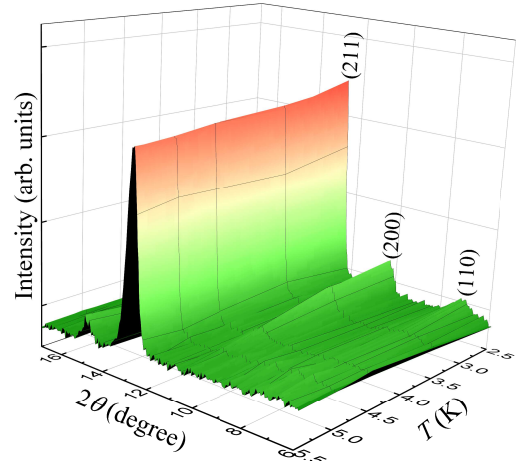


FIG. 5. 3D representation of the NPD data collected around the transitions. Only the growth of magnetic reflections are pinpointed.

substantially and the peak position shifts towards low temperatures, typical nature of AFM orderings. For $H > 1.5$ T, T_{N1} disappears completely from the measurement window while T_{N2} is shifted to 1.34 K for $H = 9$ T. This implies that the ordering at T_{N1} saturates at low fields while T_{N2} requires higher fields (> 9 T) for saturation. Concurrently, another broader maximum emerges above ~ 1.5 T and is driven higher in temperatures with increasing field. This is likely due to the redistribution of entropy where the entropy at the transition temperatures is shifted towards higher temperatures.

C. Neutron Diffraction

In order to resolve the magnetic structure, neutron powder diffraction (NPD) data are collected from 2.5 K

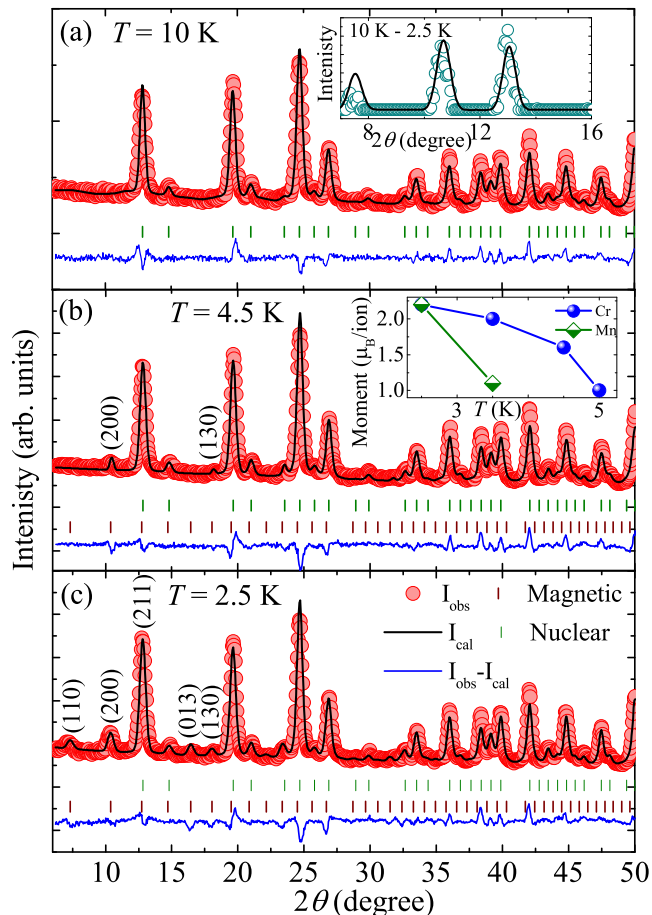


FIG. 6. The NPD data presented at three different temperatures: (a) well above the magnetic transitions (10 K) with only nuclear peaks, (b) below T_{N1} with two additional magnetic peaks, and (c) below both T_{N1} and T_{N2} , clearly showing five magnetic peaks. Rietveld fits are shown as solid black lines. Vertical bars are the allowed nuclear (top row) and magnetic (bottom row) Bragg peaks. Only the magnetic peaks in the data are indexed. Inset of (a): the difference in data between 2.5 K and 10 K highlighting only the magnetic peaks and the solid line is the Rietveld fit to the data. Inset of (b): ordered moments of Cr^{3+} and Mn^{2+} vs temperature.

to 50 K. Figure 5 presents the three-dimensional (3D) view of the temperature evaluation of low-angle peaks. At high temperatures, all the peaks are found to be arising from the nuclear reflections. At low temperatures ($T < T_{N1}$), several extra peaks with low intensity appeared, likely due to magnetic reflections. For $T < T_{N1}$, two magnetic Bragg peaks are detected at $2\theta \sim 17.98^\circ$ and $\sim 10.37^\circ$ while for $T < T_{N2}$, two more peaks are observed at $\sim 16.48^\circ$ and $\sim 7.32^\circ$ and the intensity of the nuclear peak at $\sim 12.78^\circ$ is found to be enhanced. Due to low intensity, some of the magnetic peaks are not clearly visible in the 3D plot. The individual plots in Fig. 6 highlight these peaks. The observation of magnetic reflections below T_{N1} and T_{N2} confirms two AFM transitions in MCGO.

Rietveld refinement is performed at three different temperatures, well above the magnetic transitions (10 K), below T_{N1} (4.5 K), and below T_{N2} (2.5 K) (see Fig. 6). All the peaks in the NPD data at 10 K which are nuclear in origin are well fitted by cubic crystal structure with $Ia\bar{3}d$ space group [Fig. 6(a)]. The refined lattice parameter ($a = b = c \simeq 12 \text{ \AA}$) is in close agreement with that obtained from the powder XRD data. The absence of any extra peak in the NPD data confirms single phase as well as high quality powder sample.

As shown in Fig. 6(b), the data collected at 4.5 K (i.e. below T_{N1}) shows two new peaks. Both the magnetic peaks could be indexed using a propagation vector $k = (0, 0, 0)$ and space group $I-1$. The symmetry analysis shows that these magnetic reflections can be modeled by taking the collinear AFM moment of Cr^{3+} sublattice aligned along $[1, 0, 0]$ direction. The magnetic peaks are identified to be (200) and (130). The refined magnetic structure of Cr^{3+} sub-lattice is depicted in Fig. 1(b) in which the Cr^{3+} moments in the ac -plane are aligned parallel (FM) while they are coupled antiferromagnetically along the b -direction. This confirms that below T_{N1} , Cr^{3+} sublattice is ordered in a collinear AFM fashion. Further, all the magnetic peaks in the NPD data at 2.5 K [Fig. 6(c)] could be indexed by the same propagation vector and space group by introducing the magnetic moment of the Mn^{2+} sublattice. The magnetic peaks could be indexed as (110) and (013) while the nuclear peak with enhanced intensity is identified as (211). Therefore, we conclude that T_{N2} is due to the ordering of Mn^{2+} sublattice. The ordering of Mn^{2+} sublattice is non-collinear AFM type as shown in Fig. 1(c). The solved structure of Mn^{2+} sublattice in MCGO is in close agreement with the previous report [35]. Moreover, we also performed Rietveld refinement of only the magnetic reflections obtained by taking a difference of 2.5 K and 10 K data as shown in the inset of Fig. 6(a). The magnetic moment values obtained from the refinement are consistent with the values obtained from the full dataset refinement, confirming good quality of the fit.

The obtained ordered moment for both the magnetic ions is plotted as a function of temperature in the inset of Fig. 6(b). At 2.5 K, the refined value of ordered moment of Cr^{3+} is $\mu \simeq 2.2\mu_B$ and that of Mn^{2+} is $\mu \simeq 2.2\mu_B$. These values are considerably reduced compared to the expected spin-only values $\sim 3\mu_B$ for Cr^{3+} and $\sim 5\mu_B$ for Mn^{2+} , respectively. This reduction in magnetic moment from its classical value is commonly observed in frustrated magnets [36, 37].

To investigate a possible presence of FM correlations, we have performed one-dimensional (1D) neutron depolarization measurements during which the polarization analysis of both the incident and diffracted neutron beams was performed. In these experiments, the rotation of the neutron polarization vector after transmission through the sample provides direct information about the presence and characteristics of FM correlations within the material, over a length scale of 100–1000 Å. The inset

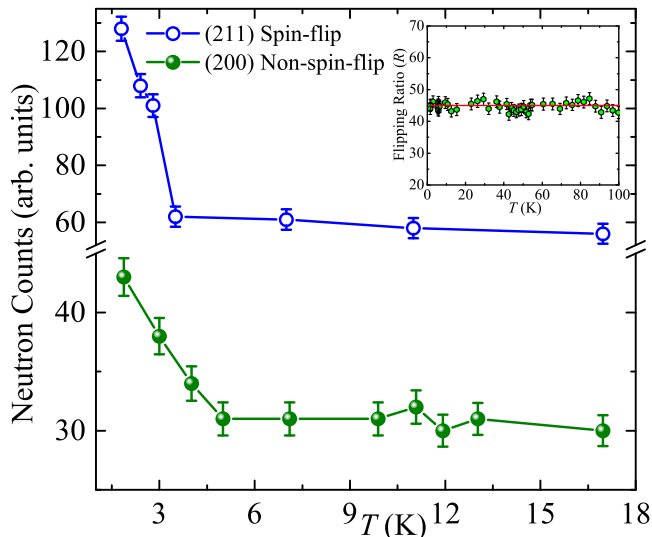


FIG. 7. Temperature dependence of magnetic reflections (200) and (211) in non-spin-flip and spin-flip channels, corresponding to Cr^{3+} and Mn^{2+} sublattices. Inset: temperature variation of flipping ratio (R) down to 1.7 K.

of Fig. 7 depicts temperature variation of flipping ratio (R) down to 1.7 K, where no depolarization of the neutron beam is observed, indicating the absence of FM or ferrimagnetic domains/clusters of the mentioned length scale under an applied field of 50 Oe. However, clusters of smaller length scales cannot be completely ruled out.

For a better understanding of the complex magnetic structure, we have measured temperature variation in the peak intensity of magnetic reflections (200) and (211) in non-spin-flip and spin-flip channels, respectively using the polarized neutron spectrometer. In this spectrometer, the neutron polarization direction is perpendicular to the scattering vector ($P \perp Q$ geometry). As we have mentioned earlier, the Bragg reflection (200) is purely magnetic and represents the ordering of Cr^{3+} sub-lattice whereas the enhanced intensity of (211) nuclear peak represents the magnetic contribution from Mn^{2+} sub-lattice. The magnetic contribution of (211) peak was confirmed by measuring the neutron intensity in the spin-flip channel. As presented in Fig. 7, the neutron counts corresponding to (200) and (211) increase abruptly below T_{N1} and T_{N2} , respectively further endorsing independent ordering of the Cr^{3+} and Mn^{2+} sub-lattices in zero-field.

It is now evident that the Cr^{3+} sub-lattice is 8-coordinated and makes a non-frustrated geometry while Mn^{2+} ions feature a frustrated hyperkagome lattice. In an ideal scenario, one would expect the Mn^{2+} sub-lattice to adopt a classical 120° ordering on each triangle [38]. In contrast, we obtained a non-collinear AFM ordering for the Mn^{2+} sub-lattice which might be due to the influence of local anisotropy, dipolar interaction etc inevitably present in experimental systems. It may also be noted that similar non-collinear magnetic structure is reported for the isostructural compound $\text{Mn}_3\text{Al}_2\text{Ge}_3\text{O}_{12}$,

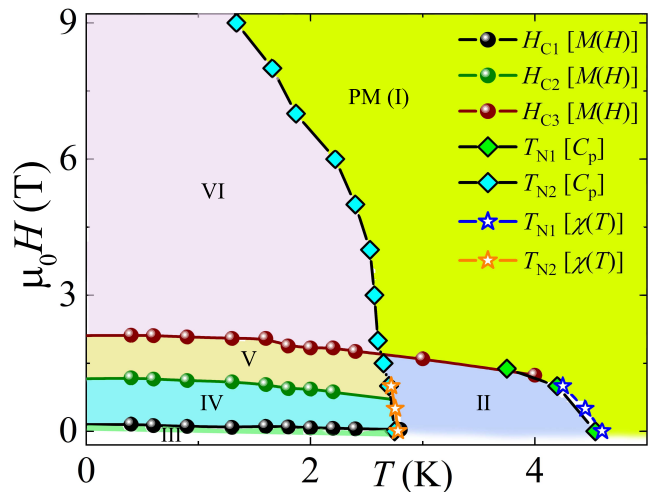


FIG. 8. $H - T$ phase diagram obtained from the magnetic isotherm, heat capacity, and susceptibility data.

with only magnetic Mn^{2+} ion. In this compound, the inelastic neutron scattering study has revealed the presence of a large variety of AFM exchange interactions mediated via one oxygen and double oxygen bonds [39]. Other garnet compounds with Co ($3d$) and Tb ($4f$) at the A site ($A_3B_2C_3O_{12}$) are also reported to show different complex AFM structures [6, 40].

For MCGO, each Mn^{2+} dodecahedron is surrounded by four edge-sharing Cr^{3+} octahedra and four edge-sharing Mn^{2+} dodecahedra. The coupling between these two sub-lattices yields a frustrated pyrochlore like structure [see Fig. 1(d)] and would reduce the gap between the two transitions. A careful scrutiny of the crystal structure reveals that there could be several interactions possible between two sub-lattices and the dominant ones are through the path $\text{Cr}^{3+} - \text{O} - \text{Mn}^{2+}$. Further, the angle $\angle \text{Mn-O-Cr}$ that provides interaction path has two values $\sim 98^\circ$ and $\sim 104^\circ$. The reduced angle ($\sim 98^\circ$) is expected to provide a FM superexchange [41]. The FM interaction is also expected for Cr^{3+} ions in the ac -plane. These observations explain the estimated small and negative value of θ_{CW} since it sums over the nearest and next-nearest neighbor interactions. Thus, the presence of both FM and AFM interactions and the intricate spin structure give rise to magnetic frustration in MCGO. Nevertheless, future inelastic neutron scattering experiments on good quality single crystals are essential to understand the magnetic interactions, origin of frustration, and the ground states.

D. Phase Diagram

The values of T_{N1} and T_{N2} obtained from $\chi(T)$ and $C_p(T)$ along with H_{C1} , H_{C2} , and H_{C3} obtained from the magnetic isotherms are summarized in Fig. 8. The $H - T$ phase diagram has six distinct phases. Phase

II and III represent the zero-field ordered states of Cr^{3+} and Mn^{2+} sub-lattices, respectively. When magnetic field is applied, three new phases (IV, V, and VI) emerge which are clearly arising due to the inter-sublattice interactions. Though the nature of these three individual phases are not known yet, this complex phase diagram can be attributed to the strongly frustrated nature of the spin system, stemming from the inter-sublattice interactions. Neutron scattering experiments in magnetic fields are required to unveil the precise nature of these phases. Similar type of complex phase diagrams are commonly found in garnet compounds due to their tangled geometry [31, 42].

E. Magnetocaloric Effect

Temperatures in the sub-Kelvin range can be attained by employing the intrinsic property of magnetic materials known as MCE [43]. In this process, first one has to apply magnetic field to the material isothermally and then remove the field adiabatically. Therefore, MCE can be quantified by the isothermal entropy change (ΔS_m) and adiabatic temperature change (ΔT_{ad}) with respect to the change in the applied field (ΔH). MCGO has two magnetic ions with high spin values ($S = 5/2$ for Mn^{2+} and $S = 3/2$ for Cr^{3+}) and double transitions at low temperatures. Hence, MCGO is expected to exhibit large ΔS_m and cooling power at low temperatures. ΔS_m can be calculated from magnetization isotherms (M vs H) measured in close temperature steps around the transitions. We can make use of Maxwell's thermodynamic relation, $(\partial S/\partial H)_T = (\partial M/\partial T)_H$, to estimate ΔS_m as [36, 44]

$$\Delta S_m(H, T) = \int_{H_i}^{H_f} \frac{dM}{dT} dH. \quad (5)$$

Figure 9(a) displays the plot of ΔS_m as a function of temperature for different ΔH values, calculated using Eq. (5). It features caret-like shape with its maximum centered around T_N , typically expected for materials with second order magnetic transition. A large MCE characterized by a maximum entropy change of $\Delta S_m \simeq -23$ J/kg-K is obtained for a field change of 7 T.

In order to cross-check the large value of ΔS_m , we have also estimated ΔS_m from the heat capacity data measured in zero-field and higher fields up to 7 T. First, we calculated the total entropy at a given field as

$$S(T)_H = \int_{T_i}^{T_f} \frac{C_p(T)_H}{T} dT, \quad (6)$$

where $C_p(T)_H$ is the heat capacity at a particular field H and T_i and T_f are the initial and final temperatures, respectively. Next, we calculated ΔS_m by taking the difference of total entropy at non-zero and zero fields as $\Delta S_m(T)_{\Delta H} = [S(T)_H - S(T)_0]_T$. Here, $S(T)_H$ and

$S(T)_0$ are the total entropy in the presence of H and in zero-field, respectively. Figure 9(b) presents the estimated ΔS_m as a function of T for different ΔH values. The shape and peak position of the curves are nearly identical to the curves obtained from the magnetic isotherms in Fig. 9(a) but with a slightly enhanced value of ΔS_m [45].

The adiabatic temperature change ΔT_{ad} can be estimated from either the combination of zero-field heat capacity and the magnetic isotherm data or the heat capacity alone measured in different magnetic fields. The estimation of ΔT_{ad} following the former method may not always give reliable results, as discussed in Ref. [33]. Therefore, we estimated ΔT_{ad} from the heat capacity data alone by taking the difference in temperatures corresponding to two different fields with same entropy value as

$$\Delta T_{\text{ad}}(T)_{\Delta H} = [T(S)_{H_f} - T(S)_{H_i}]. \quad (7)$$

ΔT_{ad} vs T for $1 \leq \Delta H \leq 7$ T calculated by this method is shown in Fig. 9(c). The maximum value at the peak position is found to be $\Delta T_{\text{ad}} \simeq 9$ K for $\Delta H = 7$ T.

Another important parameter that decides whether the material can be potentially used for magnetic refrigeration applications or not is the relative cooling power (RCP). RCP is a measure of the amount of heat transferred between the cold and hot reservoirs in a refrigeration cycle. Mathematically, it can be expressed as

$$RCP = \int_{T_{\text{cold}}}^{T_{\text{hot}}} \Delta S_m(T, H) dT, \quad (8)$$

where T_{cold} and T_{hot} correspond to temperatures of cold and hot reservoirs, respectively. The formula for RCP can be approximated as

$$|RCP|_{\text{approx}} = \Delta S_m^{\text{peak}} \times \delta T_{\text{FWHM}}, \quad (9)$$

where ΔS_m^{peak} and δT_{FWHM} are the maximum value of entropy change and full width at half maximum of the ΔS_m vs T curves, respectively. RCP as a function of H for MCGO calculated using the ΔS_m data from Fig. 9(a) is plotted in Fig. 10(a). The maximum value of RCP is obtained to be about ~ 360 J/kg for 7 T.

Magnetic cooling is a cyclic process involving repeated demagnetization of the material. Therefore, materials with a first-order phase transition are not suitable for cyclic operation because of energy loss via magnetic or thermal hysteresis [46]. Hence, materials with a second-order phase transition are better suited for commercial use. To characterize the nature of phase transition in a given material, one can further analyze the field dependence of RCP and ΔS_m^{peak} as shown in Fig. 10(a) [47]. We fitted the $RCP(H)$ and $\Delta S_m^{\text{peak}}(H)$ data by power laws of the form $RCP \propto H^N$ and $|\Delta S_m^{\text{peak}}| \propto H^n$, respectively. The values of the exponents are estimated to be $N \simeq 1.44$ and $n \simeq 1.12$. These exponents are related to the critical exponents β , γ , and δ as $N = 1 + (1/\delta)$ and

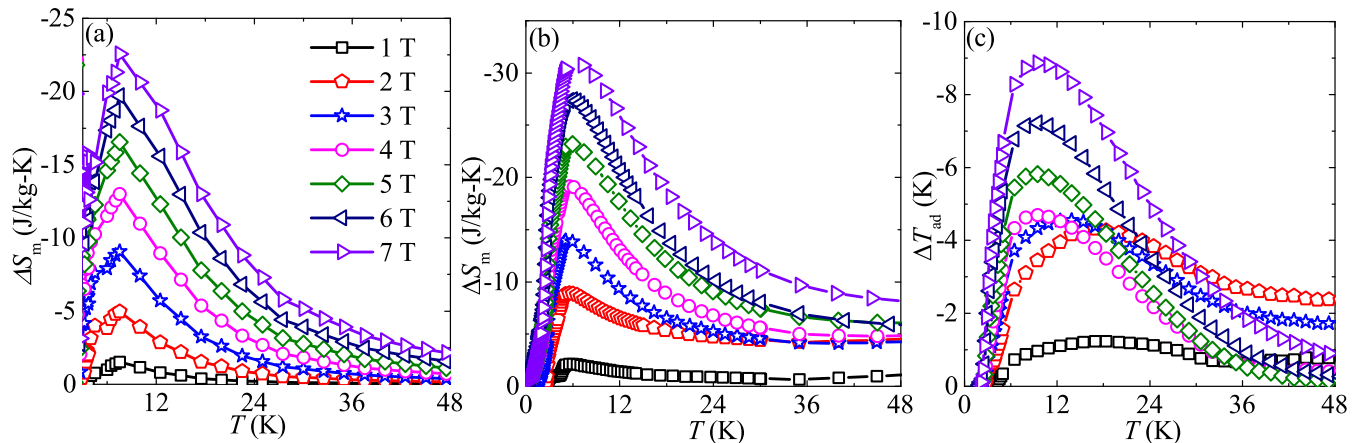


FIG. 9. (a) Entropy change (ΔS_m) as a function of T calculated for field changes $\Delta H = 1$ T to 7 T, using the magnetization data. (b) ΔS_m vs T calculated for the same ΔH values using field dependent heat capacity data. (c) Adiabatic temperature change (ΔT_{ad}) vs T calculated for the same ΔH values using heat capacity data.

$n = 1 + \frac{\beta-1}{\beta+\gamma}$. Using the value of N and n in the above relations along with the Widom formula [$\delta = 1 + (\gamma/\beta)$] give $\beta = 1.37$, $\gamma = 1.75$, and $\delta = 2.27$. These values of critical exponents do not fall under any known universality class [36].

Further, from the temperature dependence of n one can quantitatively gauge the nature of phase transition. Generally, for a second order phase transition, the exponent should have a value $n \simeq 2$ in the paramagnetic region ($T \gg T_N$), $n \simeq 1$ well below T_N , and at $T = T_N$ it depends on the critical exponents [48]. On the other hand, for a first-order phase transition, n will take a value much greater than 2 [48]. To see the variation of n with temperature, we fitted ΔS_m vs H curves at various temperatures across the transitions using the power law $\Delta S_m \propto H^n$ [see inset of Fig. 10(b)]. The obtained n vs T data is plotted in the main panel of Fig. 10(b). In the entire measured temperature range, the value of n remains below 2 with a minimum at around the transition temperatures. This confirms second-order nature of the transitions in MCGO and is suitable for cyclic operations [47].

We compared the MCE parameters of MCGO with some well-studied MCE materials having low transition temperatures in Table I. Indeed, MCGO has comparable parameters with that of other compounds. This suggests that MCGO can possibly be used in cryogenic applications to obtain sub-Kelvin temperatures. Thus, the magnetic frustration and large spin values seem to be the key factors for enhanced value of ΔS_m . Because of frustration, there is a distribution of magnetic entropy over a wide temperature range resulting in a large RCP value.

TABLE I. MCE parameters ΔT_{ad} , ΔS_m^{peak} , and RCP of some well-known magnets are compared with MCGO in a field change ΔH . The compound $\text{Li}_9\text{Cr}_3(\text{P}_2\text{O}_7)_3(\text{PO}_4)_2$ is abbreviated as LCPP.

System	T_C or T_N (K)	$ \Delta T_{ad} $ (K)	$ \Delta S_m^{\text{peak}} $ (J/kg-K)	RCP (J/kg)	ΔH (T)	Refs.
MCGO	4.5, 2.7	9	23	360	7	This work
HoMnO ₃	5	6.5	13.1	320	7	[49]
ErMn ₂ Si ₂	4.5	12.9	25.2	365	5	[50]
EdDy ₂ O ₄	5	16	25	415	8	[51]
EuHo ₂ O ₄	5	12.7	30	540	8	[51]
EuTiO ₃	5.6	21	49	500	7	[52]
LCPP	2.6	9	31	284	7	[33]

IV. SUMMARY

In summary, we reported the magnetic and magnetocaloric properties of an interesting garnet compound MCGO. It contains two magnetic sub-lattices: Mn^{2+} ($S = 5/2$) forms a geometrically frustrated hyperkagome lattice while Cr^{3+} ($S = 3/2$) forms a non-frustrated eight coordinated sub-lattice. It undergoes double transitions at $T_{N1} \sim 4.5$ K and $T_{N2} \sim 2.7$ K as clearly perceptible from the magnetization and heat capacity data. The NPD experiments confirm that these two sub-lattices order independently at low temperatures. The Cr^{3+} sub-lattice undergoes a collinear AFM ordering below T_{N1} while the Mn^{2+} sub-lattice shows the onset of a complex non-collinear AFM ordering below T_{N2} . The observed ground state also reveals a possible presence of both FM and AFM interaction between these two sub-lattices that makes a highly frustrated 3D pyrochlore geometry. The value of the ordered moments estimated from the NPD data are considerably reduced compared to the expected

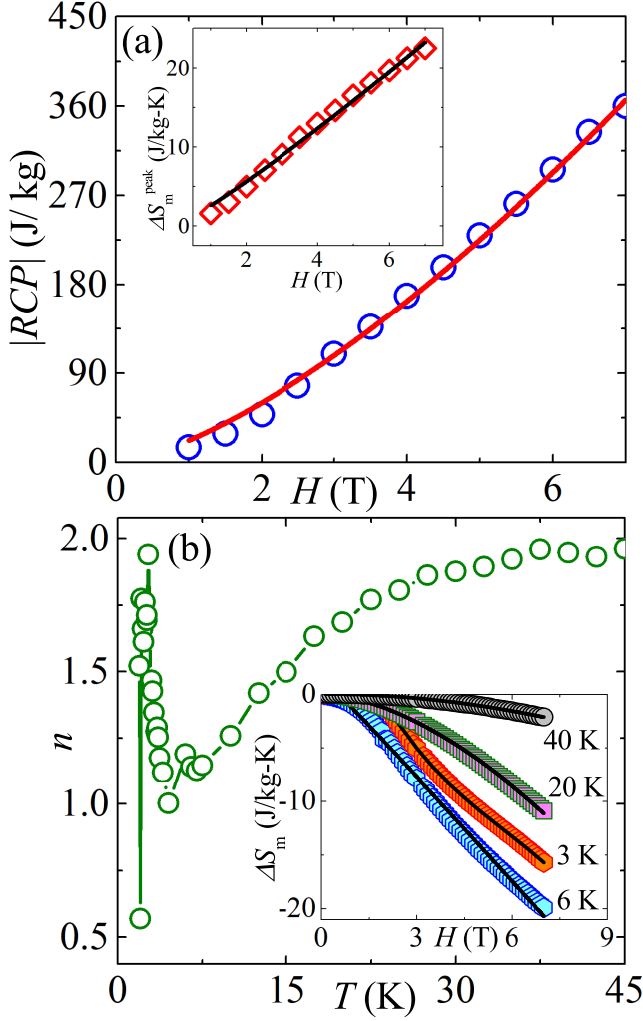


FIG. 10. (a) Relative cooling power (RCP) as a function of field (H) obtained from Fig. 9(a). Inset: peak position ΔS_m^{peak} as a function of H taken from Fig. 9(a). (b) Temperature dependence of power-law exponent n . Inset: ΔS_m vs H curves at different temperatures and solid lines represent the power law fits.

spin-only values, indicating that MCGO is a frustrated magnet. The magnetic frustration in the system might be arising from the 3D pyrochlore geometry as well as from the competing FM and AFM interactions. The coexistence of FM and AFM interactions is also inferred from the χT vs T plots. Further, multiple field-induced transitions are observed in the M vs H curves below T_{N2} , giving rise to a complex $H - T$ phase diagram. However, the exact nature of the field-induced phases are not clear yet and entails neutron diffraction experiments on good quality single crystals under magnetic fields. A large MCE characterized by large values of $\Delta S_m \sim -23$ J/kg-K, $\Delta T_{\text{ad}} \sim 9$ K, and $RCP \sim 360$ J/kg is obtained for a field change of 7 T which can be ascribed to strong frustration in the spin system. This renders MCGO as a good MCE material to achieve low temperatures by adiabatic demagnetization.

ACKNOWLEDGMENTS

For financial support, we would like to acknowledge SERB, India bearing sanction Grant No. CRG/2022/000997 and DRDO, India bearing CARS Grant No. DLJ/TC/1025/I/73.

-
- [1] O. A. Starykh, Unusual ordered phases of highly frustrated magnets: a review, *Rep. Prog. Phys.* **78**, 052502 (2015).
- [2] A. P. Ramirez, Strongly geometrically frustrated magnets, *Annu. Rev. Mater. Sci.* **24**, 453 (1994).
- [3] J. S. Gardner, M. J. P. Gingras, and J. E. Greedan, Magnetic pyrochlore oxides, *Rev. Mod. Phys.* **82**, 53 (2010).
- [4] H.-K. Jin and Y. Zhou, Classical and quantum order in hyperkagome antiferromagnets, *Phys. Rev. B* **101**, 054408 (2020).
- [5] S. Geller, Crystal chemistry of the garnets, *Zeitschrift für Kristallographie* **125**, 1 (1967).
- [6] Q. Cui, Q. Huang, J. A. Alonso, D. Sheptyakov, C. R. De la Cruz, M. T. Fernández-Díaz, N. N. Wang, Y. Q. Cai, D. Li, X. L. Dong, H. D. Zhou, and J.-G. Cheng, Complex antiferromagnetic order in the garnet $\text{Co}_3\text{Al}_2\text{Si}_3\text{O}_{12}$, *Phys. Rev. B* **101**, 144424 (2020).
- [7] J. Min, S. Zheng, J. Gong, X. Chen, F. Liu, Y. Xie, Y. Zhang, Z. Ma, M. Liu, X. Wang, H. Li, and J.-M. Liu, Magnetoelectric Effect in Garnet $\text{Mn}_3\text{Al}_2\text{Ge}_3\text{O}_{12}$, *Inorg. Chem.* **61**, 86 (2022).
- [8] J. A. M. Paddison, H. Jacobsen, Petrenko, O. A., M. T. Fernandez-Diaz, P. P. Deen, and A. L. Goodwin, Hidden order in spin-liquid $\text{Gd}_3\text{Ga}_5\text{O}_{12}$, *Science* **350**, 179 (2015).
- [9] K. Kamazawa, D. Louca, R. Morinaga, T. J. Sato, Q. Huang, J. R. D. Copley, and Y. Qiu, Field-induced antiferromagnetism and competition in the metamagnetic state of terbium gallium garnet, *Phys. Rev. B* **78**, 064412 (2008).

- [10] H. D. Zhou, C. R. Wiebe, L. Balicas, Y. J. Yo, Y. Qiu, J. R. D. Copley, and J. S. Gardner, Intrinsic spin-disordered ground state of the Ising garnet $\text{Ho}_3\text{Ga}_5\text{O}_{12}$, *Phys. Rev. B* **78**, 140406 (2008).
- [11] K. P. Belov and V. I. Sokolov, Antiferromagnetic garnets, *Sov. Phys. Usp.* **20**, 149 (1977).
- [12] Y. Kohara, Y. Yamasaki, Y. Onose, and Y. Tokura, Excess-electron induced polarization and magnetoelectric effect in yttrium iron garnet, *Phys. Rev. B* **82**, 104419 (2010).
- [13] J. Barker and G. E. W. Bauer, Thermal Spin Dynamics of Yttrium Iron Garnet, *Phys. Rev. Lett.* **117**, 217201 (2016).
- [14] R. Bozorth and S. Geller, Interactions and distributions of magnetic ions in some garnet systems, *J. Phys. Chem. Solids* **11**, 263 (1959).
- [15] B. V. M. K. P. Belov, D. G. Mamsurova and V. I. Sokolov, Ferromagnetism of the garnet $\text{Mn}_3\text{Cr}_2\text{Ge}_3\text{O}_{12}$, *JETP Lett.* **16**, 173 (1972).
- [16] T. Valyanskaya and V. Sokolov, Features of antiferromagnetic ordering in the garnet $\text{Mn}_3\text{Cr}_2\text{Ge}_3\text{O}_{12}$, *Sov. Phys. JETP* **75**, 325 (1978).
- [17] Y. Tokiwa, S. Bachus, K. Kavita, A. Jesche, A. A. Tsirlin, and P. Gegenwart, Frustrated magnet for adiabatic demagnetization cooling to milli-Kelvin temperatures, *Commun. Mater.* **2**, 42 (2021).
- [18] M. E. Zhitomirsky, Enhanced magnetocaloric effect in frustrated magnets, *Phys. Rev. B* **67**, 104421 (2003).
- [19] M. Kleinhans, K. Eibensteiner, J. Leiner, C. Resch, L. Worch, M. Wilde, J. Spallek, A. Regnat, and C. Pfeleiderer, Magnetocaloric Properties of $R_3\text{Ga}_5\text{O}_{12}$ ($R = \text{Tb}, \text{Gd}, \text{Nd}, \text{Dy}$), *Phys. Rev. Appl.* **19**, 014038 (2023).
- [20] Y. Urata, S. Wada, H. Tashiro, and P. Deng, Laser performance of highly neodymium-doped yttrium aluminum garnet crystals, *Opt. Lett.* **26**, 801 (2001).
- [21] C. Lipp, S. Strobel, F. Lissner, and R. Niewa, Garnet-type $\text{Mn}_3\text{Cr}_2(\text{GeO}_4)_3$, *Acta Cryst. E* **68**, i35 (2012).
- [22] J. R. Carvajal, Recent advances in magnetic structure determination by neutron powder diffraction, *Physica B: Condens. Matter* **192**, 55 (1993).
- [23] R. Nath, V. O. Garlea, A. I. Goldman, and D. C. Johnston, Synthesis, structure, and properties of tetragonal $\text{Sr}_2\text{M}_3\text{As}_2\text{O}_2$ ($M_3 = \text{Mn}_3, \text{Mn}_2\text{Cu}, \text{and MnZn}_2$) compounds containing alternating CuO_2 -type and FeAs -type layers, *Phys. Rev. B* **81**, 224513 (2010).
- [24] M. Subramanian, C. Torardi, D. Johnson, J. Pannetier, and A. Sleight, Ferromagnetic $R_2\text{Mn}_2\text{O}_7$ pyrochlores ($R = \text{Dy}, \text{Lu}, \text{Y}$), *J. Solid State Chem.* **72**, 24 (1988).
- [25] S. Mugiraneza and A. M. Hallas, Tutorial: a beginner's guide to interpreting magnetic susceptibility data with the Curie-Weiss law, *Commun. Phys.* **5**, 95 (2022).
- [26] J. Van Vleck, $\chi = C/(T + \Delta)$, the most overworked formula in the history of paramagnetism, *Physica* **69**, 177 (1973).
- [27] S. Mohanty, J. Babu, Y. Furukawa, and R. Nath, Structural and double magnetic transitions in the frustrated spin- $\frac{1}{2}$ capped-kagome antiferromagnet $(\text{RbCl})\text{Cu}_5\text{P}_2\text{O}_{10}$, *Phys. Rev. B* **108**, 104424 (2023).
- [28] S. Lal, S. J. Sebastian, S. S. Islam, M. P. Saravanan, M. Uhlarz, Y. Skourski, and R. Nath, Double magnetic transitions and exotic field-induced phase in the triangular lattice antiferromagnets $\text{Sr}_3\text{Co}(\text{Nb}, \text{Ta})_2\text{O}_9$, *Phys. Rev. B* **108**, 014429 (2023).
- [29] K. M. Ranjith, R. Nath, M. Majumder, D. Kasinathan, M. Skoulatos, L. Keller, Y. Skourski, M. Baenitz, and A. A. Tsirlin, Commensurate and incommensurate magnetic order in spin-1 chains stacked on the triangular lattice in $\text{Li}_2\text{NiW}_2\text{O}_8$, *Phys. Rev. B* **94**, 014415 (2016).
- [30] Y. Savina, O. Bludov, V. Pashchenko, S. L. Gnatchenko, P. Lemmens, and H. Berger, Magnetic properties of the antiferromagnetic spin- $\frac{1}{2}$ chain system $\beta\text{-TeVO}_4$, *Phys. Rev. B* **84**, 104447 (2011).
- [31] P. P. Deen, O. Florea, E. Lhotel, and H. Jacobsen, Updating the phase diagram of the archetypal frustrated magnet $\text{Gd}_3\text{Ga}_5\text{O}_{12}$, *Phys. Rev. B* **91**, 014419 (2015).
- [32] E. S. R. Gopal, *Specific Heats at Low Temperatures* (Springer, Boston, MA, 2012).
- [33] A. Magar, K. Somesh, V. Singh, J. Abraham, Y. Senyk, A. Alfonsov, B. Büchner, V. Kataev, A. Tsirlin, and R. Nath, Large Magnetocaloric Effect in the Kagome Ferromagnet $\text{Li}_9\text{Cr}_3(\text{P}_2\text{O}_7)_3(\text{PO}_4)_2$, *Phys. Rev. Appl.* **18**, 054076 (2022).
- [34] S. J. Sebastian, K. Somesh, M. Nandi, N. Ahmed, P. Bag, M. Baenitz, B. Koo, J. Sichelschmidt, A. A. Tsirlin, Y. Furukawa, and R. Nath, Quasi-one-dimensional magnetism in the spin- $\frac{1}{2}$ antiferromagnet $\text{BaNa}_2\text{Cu}(\text{VO}_4)_2$, *Phys. Rev. B* **103**, 064413 (2021).
- [35] I. Golosovskii, V. Plakhii, O. Smirnov, and Y. P. Chernenkov, Magnetic ordering of Mn^{2+} and Cr^{3+} ions in the garnet $\text{Mn}_3\text{Cr}_2\text{Ge}_3\text{O}_{12}$, *JETP Lett.* **24** (1976).
- [36] S. S. Islam, V. Singh, K. Somesh, P. K. Mukharjee, A. Jain, S. M. Yusuf, and R. Nath, Unconventional superparamagnetic behavior in the modified cubic spinel compound $\text{LiNi}_{0.5}\text{Mn}_{1.5}\text{O}_4$, *Phys. Rev. B* **102**, 134433 (2020).
- [37] S. J. Sebastian, S. S. Islam, A. Jain, S. M. Yusuf, M. Uhlarz, and R. Nath, Collinear order in the spin- $\frac{5}{2}$ triangular-lattice antiferromagnet $\text{Na}_3\text{Fe}(\text{PO}_4)_2$, *Phys. Rev. B* **105**, 104425 (2022).
- [38] J. M. Hopkinson, S. V. Isakov, H.-Y. Kee, and Y. B. Kim, Classical antiferromagnet on a hyperkagome lattice, *Phys. Rev. Lett.* **99**, 037201 (2007).
- [39] A. Gukasov, V. Plakhty, B. Dorner, S. Y. Kokovin, V. Syromyatnikov, O. Smirnov, and Y. P. Chernenkov, Inelastic neutron scattering study of spin waves in the garnet with a triangular magnetic structure, *J. Phys.: Condens. Matter* **11**, 2869 (1999).
- [40] R. Wawrzyńczak, B. Tomasello, P. Manuel, D. Khalyavin, M. D. Le, T. Guidi, A. Cervellino, T. Ziman, M. Boehm, G. J. Nilsen, and T. Fennell, Magnetic order and single-ion anisotropy in $\text{Tb}_3\text{Ga}_5\text{O}_{12}$, *Phys. Rev. B* **100**, 094442 (2019).
- [41] J. Kanamori, Superexchange interaction and symmetry properties of electron orbitals, *J. Phys. Chem. Solids* **10**, 87 (1959).
- [42] O. Florea, E. Lhotel, H. Jacobsen, C. S. Knee, and P. P. Deen, Absence of magnetic ordering and field-induced phase diagram in the gadolinium aluminum garnet, *Phys. Rev. B* **96**, 220413 (2017).
- [43] V. K. Pecharsky and K. A. Gschneidner Jr, Magnetocaloric effect and magnetic refrigeration, *J. Magn. Magn. Mater.* **200**, 44 (1999).
- [44] V. Singh, S. Sarangi, D. Samal, and R. Nath, Magnetic phase transition and magnetoelastic coupling in $\text{Fe}_{1+x}\text{Cr}_{2-x}\text{Se}_4$ ($x=0.0-0.50$), *Mater. Res. Bull.* **155**, 111941 (2022).

- [45] V. K. Pecharsky and J. Gschneidner, K. A., Magnetocaloric effect from indirect measurements: Magnetization and heat capacity, *J. Appl. Phys.* **86**, 565 (1999).
- [46] V. Franco, J.S Blázquez, B. Ingale, and A. Conde, The magnetocaloric effect and magnetic refrigeration near room temperature: Materials and models, *Annu. Rev. Mater. Res.* **42**, 305 (2012).
- [47] V. Singh, P. Bag, R. Rawat, and R. Nath, Critical behavior and magnetocaloric effect across the magnetic transition in $Mn_{1+x}Fe_{4-x}Si_3$, *Sci. Rep.* **10**, 6981 (2020).
- [48] J. Y. Law, V. Franco, L. M. Moreno-Ramírez, A. Conde, D. Y. Karpenkov, I. Radulov, K. P. Skokov, and O. Gutfleisch, A quantitative criterion for determining the order of magnetic phase transitions using the magnetocaloric effect, *Nat. Comm.* **9**, 2680 (2018).
- [49] A. Midya, P. Mandal, S. Das, S. Banerjee, L. S. S. Chandra, V. Ganesan, and S. R. Barman, Magnetocaloric effect in $HoMnO_3$ crystal, *Appl. Phys. Lett.* **96**, 142514 (2010).
- [50] L. Li, K. Nishimura, W. D. Hutchison, Z. Qian, D. Huo, and T. NamiKi, Giant reversible magnetocaloric effect in $ErMn_2Si_2$ compound with a second order magnetic phase transition, *Appl. Phys. Lett.* **100**, 152403 (2012).
- [51] A. Midya, N. Khan, D. Bhoi, and P. Mandal, Giant magnetocaloric effect in magnetically frustrated $EuHo_2O_4$ and $EuDy_2O_4$ compounds, *Appl. Phys. Lett.* **101**, 132415 (2012).
- [52] A. Midya, P. Mandal, K. Rubi, R. Chen, J.-S. Wang, R. Mahendiran, G. Lorusso, and M. Evangelisti, Large adiabatic temperature and magnetic entropy changes in $EuTiO_3$, *Phys. Rev. B* **93**, 094422 (2016)